Quantification of fibrinaloid clots in plasma from pediatric Long COVID patients using a microfluidic assay

Daniel Irimia

dirimia@mgh.harvard.edu

Massachusetts General Hospital https://orcid.org/0000-0001-7347-2082

Kirandeep Gill

Massachusetts General Hospital

Bryan Alvarez-Carcamo

Massachusetts General Hospital https://orcid.org/0009-0008-0174-5860

Carly Steifman

Massachusetts General Hospital

Zoe Swank

Massachusetts General Hospital

David Walt

Wyss Institute for Biologically Inspired Engineering https://orcid.org/0000-0002-5524-7348

Michael VanElzakker

Massachusetts General Hospital

Lael Yonker

Massachusetts General Hospital https://orcid.org/0000-0003-1711-8227

Article

Keywords:

Posted Date: October 11th, 2025

DOI: https://doi.org/10.21203/rs.3.rs-7483367/v1

Additional Declarations: There is **NO** Competing Interest.

Quantification of fibrinaloid clots in plasma from pediatric Long COVID patients using a microfluidic assay

Kirandeep K. Gill[1,2,3], Bryan Alvarez-Carcamo[4,5], Carly Steifman[4,5], Zoe Swank[2,6,7], David Walt[2,6,7], Michael B. VanElzakker[2,8,9], Lael M. Yonker[2,4,5], Daniel Irimia*[1,2,3]

[1]Center for Engineering in Medicine and Surgery, Department of Surgery, Massachusetts General Hospital, MA, USA
[2]Harvard Medical School, Boston, MA, Boston, MA, USA
[3]Shriners Children's Boston, Boston, MA, USA
[4]Department of Pediatrics, Massachusetts General Hospital, Boston, MA, USA
[5]Mucosal Immunology and Biology Research Center, Massachusetts General Hospital, Boston, MA, USA
[6]Department of Pathology, Brigham and Women's Hospital, Boston, MA, USA
[7]Wyss Institute for Biologically Inspired Engineering, Harvard University, Boston, MA, USA
[8]PolyBio Research Foundation, Boston, MA, USA
[9]Division of Neurotherapeutics, Massachusetts General Hospital, Boston, MA, USA

*dirimia@mgh.harvard.edu

Abstract

Long COVID (LC) impacts one in five children after an acute SARS-CoV-2 infection. Typical LC symptoms include fatigue, brain fog, pain, and shortness of breath, which can significantly impact individuals and society. Moreover, LC may impair school performance and have long-term health and development consequences. However, the diagnosis of LC is often imprecise and cumbersome, delaying appropriate care. To address the LC diagnosis challenges, we focused on fibrinaloid clots (microclots), recently proposed as contributing to LC's underlying mechanisms. We overcame the limitations of current microclot assessment methods, which are qualitative, by developing a microfluidic device to quantify the number of microclots in patient blood samples. We found significantly higher microclot levels in samples from pediatric LC patients than from healthy children. We evaluated the diagnostic power of the device in a cohort of 45 LC patients and 14 healthy pediatric donors. We estimated a 94% accuracy for the microclot count using the devices, significantly higher than the traditional counting of microclots on slides (66% accuracy). Intriguingly, we found the highest microclot counts in samples from patients with persistent SARS-CoV-2 spike protein in the blood. Further studies will evaluate the utility of the assay as a screening test for Long COVID in larger populations and for assessing treatment responses.

Introduction

Roughly one in five people infected with SARS-CoV-2 experience symptoms including fatigue, shortness of breath, difficulties in concentration and depressed mood, for 3 months or more after the acute infection, a condition known as long COVID (LC) or post-acute sequelae of COVID-19 (PASC) [1,2] LC affects both adults and children, often eliciting prominent endovascular symptoms such as positional orthostatic tachycardic syndrome (POTS), dizziness, and chest pain ([3,4]). However, the diagnosis of LC takes significant time because it relies on the exclusion of other conditions that share the same symptoms as LC, and because no diagnostic assay is available to validate a diagnosis. This situation delays the recognition of LC and the initiation of appropriate management, interfering with daily activities, schoolwork, sports and social interactions, with potential implications for long-term development [5,6] (**Figure 1**). Pediatric Long COVID care programs have been initiated in many countries offering physical therapy, occupational therapy and psychological support. However, these programs lack consensus concerning diagnostics and therapeutics, often derived from other post-viral syndromes, and there is a need for standardized approaches [7].

Several non-mutually exclusive hypotheses exist for LC symptoms [8], including gut dysbiosis [9], viral persistence [10], autoimmunity [11], and persistent inflammation [12] These are reflected in the guidelines for diagnostic, treatment, and monitoring of LC in children and adults [13] However, these hypotheses do not address the need for biomarkers that could facilitate a more precise LC diagnosis. Addressing this shortcoming in our understanding of LC, recent evidence suggests that the presence of fibrinaloid clots (microclots) in circulation, which are resistant to fibrinolysis, may participate in the underlying pathology of LC [14]. The evidence for elevated microclot levels in LC patients is currently based on fluorescent microscopy on glass slides. The assessment is qualitative, relying on a numerical scoring system [15,16] and typically only using five microscope fields per sample [17] Although promising, counting the microclots on slides is limited by statistical robustness and reproducibility. Alternatives are being explored. One study used flow cytometry for high-throughput analysis of microclots. However, the approach requires skilled users and high costs for specialized equipment [18]. Today, there are no standardized methods for quantifying microclots in LC [19].

Viral SARS-CoV-2 spike proteins can be detected for many months after recovery from the acute infection [20–22]. The spike protein is considered critical in thrombosis pathogenesis, leading to the formation of amyloid fibrin networks and the development of microclots [23]. The presence of circulating SARS-CoV-2 spike protein in the blood (spike antigenemia) has been detected in LC patients, implying a reservoir of active virus or components of the virus [24]. Platelet-neutrophil interplay is also a key mechanism of immunothrombosis, primarily mediated by the formation of neutrophil extracellular traps [25]. The accepted mechanism for the formation of microclots is complex and results from upregulated coagulation, stimulated inflammatory reactions, endothelial dysfunction and activated monocytes and platelets [26–28]. The study of microclots revealed intriguing correlations with symptom severity, disease progression, and efficacy of therapeutic interventions [29].

In this paper, we present a microfluidic device to assess microclot burden in blood samples from LC patients quantitatively. This development and validation of the device could potentially lead to new biomarkers that could enable faster LC diagnosis, precise monitoring of LC progression, and add objective metrics to studies of the effectiveness of emerging therapeutic interventions in LC.

Materials and methods

Collection of plasma samples

To mitigate risk of age-related inflammatory or coagulopathy disorders, we enrolled healthy pediatric participants (n = 14) and children and young adults with LC (n = 45), per guidelines from the Centers for Disease Control (CDC), under the institutional review board (IRB) approved "MGH Pediatric COVID-19 Biorepository" (IRB# 2020P000955). Participants classified as healthy controls did not present with clinical signs of infection or illness based on previous medical history reviews. We obtained informed consent from participants or guardians prior to enrollment in accordance with IRB-approved guidelines. We collected blood for microclot quantification and then centrifuged the blood to collect the platelet-poor plasma layer and stored samples at –80°C in microcentrifuge tubes (Sigma Aldrich). We also tested LC participants for the presence of SARS-CoV-2 spike antigenemia in circulation.

Microfluidic device fabrication

We photopatterned microfluidic designs onto a 4" silicon wafer using mylar masks (Fineline, Colorado Springs, CO) and SU-100 photoresist (MicroChem, Newton, MA) using standard photolithography. The height of the microchannels were 200 µm. We poured a mixture of polydimethylsiloxane prepolymer (PDMS, Corning, Corning, NY) and curing agent with a 10:1 weight ratio onto the SU-8 wafer to a 3 mm thickness. We then degassed the mixture at room temperature under vacuum for one hour and placed the wafer into an oven at 80 °C overnight. We punched holes into the cured PDMS using a 1.2 mm biopsy punch for fluid inlet and outlets in the microchannels. Finally, we treated PDMS and glass slides with oxygen plasma, plasma-bonded the materials together and then heated the bonded device for 10 minutes at 85 °C.

Staining microclots in plasma samples

Plasma samples were stored at -80 °C. On the day of processing, we thawed samples and centrifuged them at 450 RCF using a high stoppage for 15 minutes. We stained microclots in the plasma samples using 100 µM Thioflavin T (ThT, Sigma Aldrich) [19]and incubated the samples in the dark for 30 minutes at room temperature.

Loading plasma samples into microfluidic devices

We captured microclots in the device using a two-step flow process. For the first fast flow step, we took 6 µL of the plasma sample and loaded it into the device by pipetting it into the inlet. We then placed a large droplet of PBS (Sigma Aldrich, ~20 µL) on top of the outlet to act as a fluid reservoir. In the second slow flow step, we added a smaller PBS droplet (~6 µL) on top of the inlet to drive the flow of microclots into the channel using passive fluid flow via Laplace pressure differences.

Loading plasma samples on microscopy glass slides

We pipetted a 5 µL aliquot of plasma onto the center of a glass slide and then placed a coverslip on top to evenly distribute the sample. We then allowed the slide to sit at room temperature for 30 minutes to facilitate settling and adhesion of microclots.

Image acquisition and processing

We imaged microclots using x20 magnification with a Nikon TiE widefield microscope (Micro Video Instruments, Avon, MA, USA) and NIS Elements software. We imaged the microfluidic devices at a single z-stack and the slides at multiple z-stacks. We used the FITC fluorescence filter to visualize microclots. We quantified microclots using the Particle Analyzer tool in the ImageJ software (National Institute of Health). These tools helped to determine microclot counts and assess sizes. We set a minimum area of 10 μm^2 for analysis.

Statistics

We performed graphing and statistical analysis using Graphpad Prism 9 software and analyzed outcomes using a t-test to compare the outcomes of 2 groups or ordinary one-way ANOVA to compare the outcomes of more than 2 groups. A P-value > 0.05 was determined to be not significant. P-values for significant differences were labeled as follows: * for $P < 0.05$, ** for $P < 0.01$, *** for $P < 0.001$, and **** for $P < 0.0001$.

Results

Study design

We measured microclots in platelet-poor plasma samples from 59 participants, of which 45 participants were diagnosed with LC and 14 participants were healthy donors. To mitigate the risk of confounding age-related inflammatory disease, which can activate pro-coagulopathic and thromboembolic pathways, we primarily enrolled children and young adults (mean age for healthy control was 8.3 years; 17 years for LC). Among the LC group, 7 patient samples tested positive for spike antigenemia (LC+). LC plasma samples were collected from March 2023 to November 2024. We also tested plasma samples that were collected from healthy donors in 2021, when the incidence of LC was still low. Details of participants, including age, sex, and ethnicity, are shown in **Table 1**.

Design of microfluidic devices

We designed a device to capture and help count microclots from plasma samples. The device can accommodate microclots up to 200 μm in diameter, compatible with the 1 to 200 μm microclot size range reported in previous studies [19]. Our microfluidic channel had a height of 200 μm, a width of 1,200 μm, and a length of 6,700 μm (**Figure 2A**). The height of the device allowed microclots to settle quickly, which enabled imaging in a single z-plane for fast image acquisition. We observed significant variations in microclot morphology, ranging from circular to elongated shapes (**Figure 2B**). We designed the device as long channels **(Figure 2C)** to enable scalability and parallel processing, where up to 18 channels could be fitted on a single glass slide.

Surface-tension-driven fluid flow

We used a two-step flow process to capture microclots in the devices. We first introduced a 6 μL plasma sample into the inlet using a pipette, pushing the sample through the device in a fast flow step, at ~3 μL/s. At the end of this step, both the inlet and the outlet of the device were filled with plasma all the way to the top of the device. Then, we placed a 20 μL drop of phosphate buffer solution (PBS) over the outlet, in contact with the plasma column inside the outlet. Then, we placed another 6 μL PBS drop over the inlet, in contact with the plasma inside the inlet. Fluid flow stopped when the inlet droplet spread and reached a radius equal to that of the outlet droplet. The difference in the size of the droplets at the inlet and outlet is responsible for slow, surface-tension driven fluid flow of the plasma sample through the channel at ~0.2 μL/s.

The slow flow of the second step is driven by capillary force differences at the inlet and outlet and follows the Young-Laplace equation, which describes the pressure difference across the interface of a curved surface with a radius, R, due to surface tension (γ). A smaller droplet will therefore have a higher internal pressure compared to a larger droplet. By creating a pressure gradient using two droplets of different sizes, fluid will passively flow from a higher pressure toward a lower pressure through a conduit **(Figure 3A)**. We demonstrated this principle using PBS stained with blue dye, which allows the movement of the fluid along the channel to be monitored (**Figure 3B, Supplementary Video V1**). By tracking the fluid front of the dye along the channel length from the inlet to the outlet during flow, we observed a linear flow rate with a velocity of 15 mm/s (**Figure 3C-D**).

High efficiency microclot capture with uniform spatial distribution

We analyzed the number of microclots in the channel of the device compared to the inlet and outlet and found that 83 ± 5.9 % of microclots were captured per channel (**Figure 3E**). A higher number of microclots were also observed in the outlet compared to the inlet, confirming the passive pumping of microclots from the inlet. Next, we studied the distribution of microclots

within the channel. We counted the number of microclots across the channel width and analyzed their cumulative distribution along the channel length. We observed a linear distribution of microclots along the channels, indicating an even capture efficiency along the length of the channel (**Figure 3F**).

To study flow dynamics further, we analyzed fluid flow in the device loaded with plasma and observed significantly slower flow rates than in a device loaded with PBS fluid (**Figure 4A**). These were likely due to the higher viscosity of plasma, which would reduce flow rate in accordance with the Hagen-Poiseuille equation **(Figure 4B)**. A velocity of 0.65 mm/s was obtained with the plasma fluid, accompanied by a delay in the dye reaching the front of the inlet as the fluid took a longer time travelling down the inlet stream in the y-direction (**Figure 4C**). This slowed fluid movement likely contributed to Taylor–Aris dispersion, where initial parabolic flow due to convection, typical of microfluidic systems, gradually spreads towards the channel walls through lateral diffusion **(Figure 4D)**. We also tested gravity settling of microclots over time and observed no positional changes, confirming that microclots could be imaged in a single z-plane at high-resolution (**Figure 4E**).

Elevated microclot burden in LC samples

Following validation of the microfluidic device's performance, we proceeded to optimize the number of channels needed per sample. We tested channel numbers ranging from 2 to 8, comparing LC samples and healthy controls, and found that a minimum of four channels was needed to achieve statistical confidence **(Figure 5)**. Consequently, we analyzed all samples using four channels per sample. We observed a higher quantity of microclots in LC samples with an average of 166.1 $\pm$ 106.7 microclots/sample (mean +/- standard deviation; N=180 channels) compared to 60.8 $\pm$ 47.7 microclots/sample (N=56 channels) in the healthy controls (**Figure 6A**). We also quantified samples by taking the average of 4 channels per sample and observed the same trend (**Figure 6B**).

Spike antigenemia associated with increased microclot burden in LC patients

Our analysis revealed higher microclot burdens in LC (+) plasma samples with an average of 229.2 +/- 110.9 (N=28 channels) compared to 154.4 +/- 102.1 (N=152 channels) in LC (-) samples (**Figure 6A**). We observed a saturation threshold of ~500 microclots in a single channel with exceptionally high microclot loads. This threshold was high enough to differentiate between the microclot burden across samples.

Larger microclot sizes within areas up to 100 μm^2

We measured no significant differences in the average size of microclots in samples from LC and HC subjects (**Figure 6C**). To study the microclot size in more detail, a histogram was plotted to show the distribution of microclot sizes. Most microclots in both LC and HC samples fell in the 10 – 30 μm^2 size range, with the upper limit observed to be 100 μm^2 (**Figure 6D**). When the total microclot count was matched between LC and HC samples, the size distribution of microclots was similar across both groups (**Figure 6E**). Based on this, we set the analysis range to $\leq$100 μm^2 and observed larger microclot sizes in LC samples compared to HC samples (**Figure 6F**).

Higher microclot counts in microfluidic devices compared to traditional glass slides

To benchmark performance, we compared microclot count and area for LC and HC samples obtained using the microfluidic device with the slide method. Higher microclot counts were observed in the microfluidic devices compared to the glass slides (**Figure 7A**). LC samples had a mean count of 31.5 $\pm$ 19.6 microclots/sample (N = 45 samples) with the slides compared to a five-fold increase of 161.4 $\pm$ 91.4 microclots/sample (N = 39 samples) in the devices.

Larger microclot sizes were observed in the slides compared to the devices (**Figure 7B**). The mean microclot area in LC samples with the slides was 331.1 ± 240.0 μm² compared to 199.8 ± 69.0 μm² in the HC samples. This difference was also apparent in the range of microclot areas, which was 1163.0 μm² and 261.7 μm² for LC and HC samples, respectively, with the slides. Comparatively, the range for the microclot area entering the channels was limited by the height of the channels and observed to be 165.3 μm² and 162.7 μm² for LC and HC samples, respectively.

Receiver operating curves to determine optimal microclot threshold value

To evaluate the diagnostic accuracy of the device, we used receiver operating characteristic (ROC) curves, which plot sensitivity against 1 − specificity, to determine the optimal threshold value for distinguishing LC and HC samples. The overall accuracy of the test can be summarized using the Area Under the Curve (AUC).

For microclots counted using the microfluidic devices, we calculated an optimal threshold of 75 microclots/sample for differentiating between LC and HC samples, corresponding to a sensitivity of 91% and specificity of 86% (**Figure 8**). Comparatively, when we used the slide method as previously described [19], we determined an optimal threshold at 23 microclots/sample, for a sensitivity of 61% and specificity of 57%. The AUC was 0.94 and 0.66 for the microfluidic devices and slides, respectively. The ROC analysis for the size of the microclots with the slides was comparable with an AUC of 0.67. To study the ROC for the microfluidic device in more detail, we investigated LC (+) only and LC (-) only samples and found that the device performed equally well for both groups (**Figure 8C-D**). LC (+) samples had an AUC of 0.93 with a sensitivity of 89% and a specificity of 86%. LC (-) samples had an AUC of 0.82 with a sensitivity of 72% and a specificity of 71%.

Discussion

This work introduces a microfluidic device to quantify the amount of microclots in pediatric blood samples. The device operates using a two-step flow process, firstly by introducing the sample using a pipette in a fast flow step and secondly using a slow flow step through passive fluid flow via Laplace pressure differences. The slower velocity in the second step increases the capture efficiency and distributes the microclots along the capture channel.

Surface tension properties present at the microfluidic scale can be applied to drive flow using passive and precise fluid control. Surface tension-driven flow by leveraging the pressure differential between two droplets [30] is amenable to biological experimentation and has been applied to microfluidic technologies to study cell culture [31], functional cytomics for hematologic cancers [32] and cardiotoxicity assays [33]. We applied droplet-based passive pumping to our microclot quantification device, enabling rapid setup and easy integration. We observed linear velocity from fluid flow characterization experiments, in line with findings from previous studies [34], providing an even spatial distribution of microclots across the microfluidic channel.

We observed an increased microclot burden in LC samples compared to healthy controls. The measured differences correspond to an accuracy of 94% in differentiating LC and HC samples. This was significantly higher than the current method of assessing microclots on slides, which in our hands, had an accuracy of 66%. The majority of microclots in the devices had areas in the 10–30 μm^2 range, consistent with previous slide-based studies [19,29]. Overall, these results suggest that the microfluidic channel and protocol have the potential to serve as diagnostic assays in LC. Larger studies will be required to strengthen our initial findings, including patients with various inflammatory conditions that may also increase the number of microclots. The simplicity of the device architecture and the use of passive-flow control should enable large-scale manufacturing for scalable, low-cost production of the diagnostic platform.

The increased microclot burden occurred in all LC patients, including both those with detectable and those without detectable Spike protein in their blood. A possible explanation is that the presence of Spike in patients with LC symptoms may vary over time around the limit of protein detection (10–60%) [35] and Spike levels entering circulation [36]. The ability of the microfluidic device to differentiate LC subgroups with and without detectable Spike antigenemia further reinforces the potential utility of microclot measurement in LC. However, the clinical impact of detecting microclots in the blood of patients with LC remains unclear. Based on our current understanding of microclot composition, traditional anticoagulants or fibrinolytic interventions are ineffective against microclots. Thus, the detection of microclots should not drive decisions to treat with anticoagulants or other similar interventions. Nonetheless, the ability to measure microclots may enable monitoring of LC patients and evaluation of future therapeutic interventions targeting thrombo-inflammatory pathways.

In conclusion, we present a microfluidic device to quantify microclots in LC patients with high sensitivity and specificity, supporting the promise of microclot burden serving as a biomarker for LC. Future studies in larger and more diverse populations of patients are needed to confirm the potential of our approach for diagnostic, monitoring, and treatment in LC.

Author contributions

K.K.G and D.I designed and conducted the study. K.K.G designed the microfluidic device. L.M.Y acquired pediatric clinical samples. K.K.G and B.A conducted experiments. K.K.G performed data analysis and drafted the manuscript. L.M.Y, M.B.V, and D.I contributed to editing the manuscript. L.M.Y, M.B.V, and D.I. obtained funding support.

Acknowledgments

We are thankful for the support from PolyBio Research Foundation and Wallace Foundation. Microfabrication was performed at the BioMEMS Core at the Massachusetts General Hospital. We are also thankful to Etheresia Pretorius, Ph.D. and Amy Proal, Ph.D., for early help in implementing the microclot assay in our lab.

Disclosures

The authors have stated that there are no conflicts of interest.

References

[1] S. Rao, R.S. Gross, S. Mohandas, C.R. Stein, A. Case, B. Dreyer, N.M. Pajor, H.T. Bunnell, D. Warburton, E. Berg, J.B. Overdevest, M. Gorelik, J. Milner, S. Saxena, R. Jhaveri, J.C. Wood, K.E. Rhee, R. Letts, C. Maughan, N. Guthe, L. Castro-Baucom, M.S. Stockwell, Postacute Sequelae of SARS-CoV-2 in Children, Pediatrics 153 (2024) e2023062570. https://doi.org/10.1542/peds.2023-062570.

[2] Long COVID, National Center for Health Statistics. U.S. Census Bureau, Household Pulse Survey, Https://Www.Cdc.Gov/Nchs/Covid19/Pulse/Long-Covid.Htm (2022).

[3] C.K. Ormiston, I. Świątkiewicz, P.R. Taub, Postural orthostatic tachycardia syndrome as a sequela of COVID-19, Heart Rhythm 19 (2022) 1880–1889. https://doi.org/https://doi.org/10.1016/j.hrthm.2022.07.014.

[4] Y.-X. Cui, J.-B. Du, H.-F. Jin, Insights into postural orthostatic tachycardia syndrome after COVID-19 in pediatric patients, World Journal of Pediatrics 20 (2024) 201–207. https://doi.org/10.1007/s12519-024-00796-0.

[5] L.C.E. Noij, C.R. Lap, M.A.J. Luijten, S. Hashimoto, L. Teela, K.J. Oostrom, M.W. Alsem, M.A. van Houten, G. Biesbroek, L. Haverman, A.H. Maitland-van der Zee, J.B. van Goudoever, S.W.J. Terheggen-Lagro, Quality of life and mental health in children with long COVID, Communications Medicine 5 (2025) 271. https://doi.org/10.1038/s43856-025-00947-y.

[6] R.S. Gross, T. Thaweethai, L.C. Kleinman, J.N. Snowden, E.B. Rosenzweig, J.D. Milner, K.G. Tantisira, K.E. Rhee, T.L. Jernigan, P.A. Kinser, A.L. Salisbury, D. Warburton, S. Mohandas, J.C. Wood, J.W. Newburger, D.T. Truong, V.J. Flaherman, T.D. Metz, E.W. Karlson, L.B. Chibnik, D.B. Pant, A. Krishnamoorthy, R. Gallagher, M.F. Lamendola-Essel, D.C. Hasson, S.D. Katz, S. Yin, B.P. Dreyer, M. Carmilani, K. Coombs, M.L. Fitzgerald, N. Güthe, M. Hornig, R.J. Letts, A.K. Peddie, B.D. Taylor, A.S. Foulkes, M.S. Stockwell, R.-P. Consortium, R.-P.G. Authors, Characterizing Long COVID in Children and Adolescents, JAMA 332 (2024) 1174–1188. https://doi.org/10.1001/jama.2024.12747.

[7] C.L.H. Brackel, L.C.E. Noij, S.J.H. Vijverberg, C.L. Legghe, A.H. Maitland-van der Zee, J.B. van Goudoever, D. Buonsenso, D. Munblit, L. Sigfrid, S. McFarland, L. Anmyr, L. Ashkenazi-Hoffnung, A.P.N. Bellinat, N.L.S. Dias, A. Edwards, T. Fashina, R.G. Juraški, A.L.N. Gonçalves, E. Hansted, V. Herczeg, O. Hertting, L.N. Jankauskaite, N. Kaswandani, R. Kevalas, P. Krivácsy, M. Lorenz, L.A. Malone, M. McVoy, D.W. Miller, A.K. Morrow, M.D. Nugawela, C.R. Oliveira, P.R.S. Oliveira, I.M. Osmanov, I.M. Overmars, E. Paintsil, S.M. Pinto Pereira, Y. Prawira, N.D. Putri, R.C.F. Ramos, M. Rasche, M. Ryd-Rinder, C. De Rose, E. Samitova, T.S. Jovanović, D. Say, J.T. Scott, I. Shachar-Lavie, R. Shafran, E. Shmueli, A. Snipaitiene, T. Stephenson, N. Ténai, S. Tosif, M. Turkalj, P. Valentini, L.R.S. Vasconcelos, L. Villard, D. Vilser, S. Hashimoto, S.W.J. Terheggen-Lagro, International Care programs for Pediatric Post-COVID Condition (Long COVID) and the way forward, Pediatr Res 96 (2024) 319–324. https://doi.org/10.1038/s41390-023-03015-0.

[8] A.D. Proal, M.B. VanElzakker, Long COVID or Post-acute Sequelae of COVID-19 (PASC): An Overview of Biological Factors That May Contribute to Persistent Symptoms, Front Microbiol 12 (2021). https://doi.org/10.3389/fmicb.2021.698169.

[9] N.T. Iqbal, H. Khan, A. Khalid, S.F. Mahmood, N. Nasir, I. Khanum, I. de Siqueira, W. Van Voorhis, Chronic inflammation in post-acute sequelae of COVID-19 modulates gut microbiome: a review of literature on COVID-19 sequelae and gut dysbiosis, Molecular Medicine 31 (2025) 22. https://doi.org/10.1186/s10020-024-00986-6.

[10] A.D. Proal, M.B. VanElzakker, S. Aleman, K. Bach, B.P. Boribong, M. Buggert, S. Cherry, D.S. Chertow, H.E. Davies, C.L. Dupont, S.G. Deeks, W. Eimer, E.W. Ely, A. Fasano, M. Freire, L.N. Geng, D.E. Griffin, T.J. Henrich, A. Iwasaki, D. Izquierdo-Garcia, M. Locci, S.

Mehandru, M.M. Painter, M.J. Peluso, E. Pretorius, D.A. Price, D. Putrino, R.H. Scheuermann, G.S. Tan, R.E. Tanzi, H.F. VanBrocklin, L.M. Yonker, E.J. Wherry, SARS-CoV-2 reservoir in post-acute sequelae of COVID-19 (PASC), Nat Immunol 24 (2023) 1616–1627. https://doi.org/10.1038/s41590-023-01601-2.

[11] S. Talwar, J.A. Harker, P.J.M. Openshaw, R.S. Thwaites, Autoimmunity in long COVID, Journal of Allergy and Clinical Immunology 155 (2025) 1082–1094. https://doi.org/https://doi.org/10.1016/j.jaci.2025.02.005.

[12] S. Mehandru, M. Merad, Pathological sequelae of long-haul COVID, Nat Immunol 23 (2022) 194–202. https://doi.org/10.1038/s41590-021-01104-y.

[13] S. Lopez-Leon, T. Wegman-Ostrosky, N.C. Ayuzo del Valle, C. Perelman, R. Sepulveda, P.A. Rebolledo, A. Cuapio, S. Villapol, Long-COVID in children and adolescents: a systematic review and meta-analyses, Sci Rep 12 (2022) 9950. https://doi.org/10.1038/s41598-022-13495-5.

[14] D.M. Altmann, E.M. Whettlock, S. Liu, D.J. Arachchillage, R.J. Boyton, The immunology of long COVID, Nat Rev Immunol 23 (2023) 618–634. https://doi.org/10.1038/s41577-023-00904-7.

[15] G.J. Laubscher, P.J. Lourens, C. Venter, D.B. Kell, E. Pretorius, TEG®, microclot and platelet mapping for guiding early management of severe COVID-19 coagulopathy, J Clin Med 10 (2021). https://doi.org/10.3390/jcm10225381.

[16] A. Kruger, M. Vlok, S. Turner, C. Venter, G.J. Laubscher, D.B. Kell, E. Pretorius, Proteomics of fibrin amyloid microclots in long COVID/post-acute sequelae of COVID-19 (PASC) shows many entrapped pro-inflammatory molecules that may also contribute to a failed fibrinolytic system, Cardiovasc Diabetol 21 (2022) 190. https://doi.org/10.1186/s12933-022-01623-4.

[17] J. Schofield, S.T. Abrams, R. Jenkins, S. Lane, G. Wang, C.-H. Toh, Microclots, as defined by amyloid-fibrinogen aggregates, predict risks of disseminated intravascular coagulation and mortality, Blood Adv 8 (2024) 2499–2508. https://doi.org/10.1182/bloodadvances.2023012473.

[18] S. Turner, G.J. Laubscher, M.A. Khan, D.B. Kell, E. Pretorius, Accelerating discovery: A novel flow cytometric method for detecting fibrin(ogen) amyloid microclots using long COVID as a model, Heliyon 9 (2023). https://doi.org/10.1016/j.heliyon.2023.e19605.

[19] D.B. Kell, G.J. Laubscher, E. Pretorius, A central role for amyloid fibrin microclots in long COVID/PASC: origins and therapeutic implications, Biochemical Journal 479 (2022) 537–559. https://doi.org/10.1042/BCJ20220016.

[20] C.C.L. Cheung, D. Goh, X. Lim, T.Z. Tien, J.C.T. Lim, J.N. Lee, B. Tan, Z.E.A. Tay, W.Y. Wan, E.X. Chen, S.N. Nerurkar, S. Loong, P.C. Cheow, C.Y. Chan, Y.X. Koh, T.T. Tan, S. Kalimuddin, W.M.D. Tai, J.L. Ng, J.G.-H. Low, J. Yeong, K.H. Lim, Residual SARS-CoV-2 viral antigens detected in GI and hepatic tissues from five recovered patients with COVID-19, Gut 71 (2022) 226. https://doi.org/10.1136/gutjnl-2021-324280.

[21] S.R. Stein, S.C. Ramelli, A. Grazioli, J.-Y. Chung, M. Singh, C.K. Yinda, C.W. Winkler, J. Sun, J.M. Dickey, K. Ylaya, S.H. Ko, A.P. Platt, P.D. Burbelo, M. Quezado, S. Pittaluga, M. Purcell, V.J. Munster, F. Belinky, M.J. Ramos-Benitez, E.A. Boritz, I.A. Lach, D.L. Herr, J. Rabin, K.K. Saharia, R.J. Madathil, A. Tabatabai, S. Soherwardi, M.T. McCurdy, A.L. Babyak, L.J. Perez Valencia, S.J. Curran, M.E. Richert, W.J. Young, S.P. Young, B. Gasmi, M. Sampaio De Melo, S. Desar, S. Tadros, N. Nasir, X. Jin, S. Rajan, E. Dikoglu, N. Ozkaya, G. Smith, E.R. Emanuel, B.L. Kelsall, J.A. Olivera, M. Blawas, R.A. Star, N. Hays, S. Singireddy, J. Wu, K. Raja, R. Curto, J.E. Chung, A.J. Borth, K.A. Bowers, A.M. Weichold, P.A. Minor, M.A.N. Moshref, E.E. Kelly, M.M. Sajadi, T.M. Scalea, D. Tran, S. Dahi, K.B. Deatrick, E.M. Krause, J.A. Herrold, E.S. Hochberg, C.R. Cornachione, A.R. Levine, J.E. Richards, J. Elder, A.P. Burke, M.A. Mazzeffi, R.H. Christenson, Z.A. Chancer, M. Abdulmahdi, S. Sopha, T. Goldberg, Y. Sangwan, K. Sudano, D. Blume, B.

Radin, M. Arnouk, J.W. Eagan, R. Palermo, A.D. Harris, T. Pohida, M. Garmendia-Cedillos, G. Dold, E. Saglio, P. Pham, K.E. Peterson, J.I. Cohen, E. de Wit, K.M. Vannella, S.M. Hewitt, D.E. Kleiner, D.S. Chertow, N.I.H.C.-19 A. Consortium, SARS-CoV-2 infection and persistence in the human body and brain at autopsy, Nature 612 (2022) 758–763. https://doi.org/10.1038/s41586-022-05542-y.

[22] M.J. Peluso, Z.N. Swank, S.A. Goldberg, S. Lu, T. Dalhuisen, E. Borberg, Y. Senussi, M.A. Luna, C. Chang Song, A. Clark, A. Zamora, M. Lew, B. Viswanathan, B. Huang, K. Anglin, R. Hoh, P.Y. Hsue, M.S. Durstenfeld, M.A. Spinelli, D. V Glidden, T.J. Henrich, J.D. Kelly, S.G. Deeks, D.R. Walt, J.N. Martin, Plasma-based antigen persistence in the post-acute phase of COVID-19, Lancet Infect Dis 24 (2024) e345–e347. https://doi.org/https://doi.org/10.1016/S1473-3099(24)00211-1.

[23] T.C. Iba Jean M.; Levy Jerrold H., What Role Does Microthrombosis Play in Long COVID?, Semin Thromb Hemost 50 (2023) 527–536. https://doi.org/10.1055/s-0043-1774795.

[24] Z. Swank, Y. Senussi, Z. Manickas-Hill, X.G. Yu, J.Z. Li, G. Alter, D.R. Walt, Persistent Circulating Severe Acute Respiratory Syndrome Coronavirus 2 Spike Is Associated With Post-acute Coronavirus Disease 2019 Sequelae, Clinical Infectious Diseases 76 (2023) e487–e490. https://doi.org/10.1093/cid/ciac722.

[25] L.L. Nicolai A; Brambs S, Immunothrombotic dysregulation in COVID-19 pneumonia is associated with respiratory failure and coagulopathy, Circulation 142 (2020) 1176–1189. https://doi.org/10.1161/CIRCULATIONAHA.120.048488.

[26] J.M. Connors, T. Iba, R.T. Gandhi, Thrombosis and Coronavirus Disease 2019: Controversies and (Tentative) Conclusions, Clinical Infectious Diseases 73 (2021) 2294–2297. https://doi.org/10.1093/cid/ciab096.

[27] E.I. Obeagu, G.U. Obeagu, Thromboinflammation in COVID-19: Unraveling the interplay of coagulation and inflammation, Medicine 103 (2024). https://journals.lww.com/md-journal/fulltext/2024/07120/thromboinflammation_in_covid_19__unraveling_the.71.aspx.

[28] L. Nicolai, R. Kaiser, K. Stark, Thromboinflammation in long COVID—the elusive key to postinfection sequelae?, Journal of Thrombosis and Haemostasis 21 (2023) 2020–2031. https://doi.org/10.1016/j.jtha.2023.04.039.

[29] E. Pretorius, C. Venter, G.J. Laubscher, P.J. Lourens, J. Steenkamp, D.B. Kell, Prevalence of readily detected amyloid blood clots in ‘unclotted’ Type 2 Diabetes Mellitus and COVID-19 plasma: a preliminary report, Cardiovasc Diabetol 19 (2020). https://doi.org/10.1186/s12933-020-01165-7.

[30] P.J. Resto, E. Berthier, D.J. Beebe, J.C. Williams, An inertia enhanced passive pumping mechanism for fluid flow in microfluidic devices, Lab Chip 12 (2012) 2221–2228. https://doi.org/10.1039/C2LC20858J.

[31] I. Meyvantsson, J.W. Warrick, S. Hayes, A. Skoien, D.J. Beebe, Automated cell culture in high density tubeless microfluidic device arrays, Lab Chip 8 (2008) 717–724. https://doi.org/10.1039/B715375A.

[32] E.W.K. Young, C. Pak, B.S. Kahl, D.T. Yang, N.S. Callander, S. Miyamoto, D.J. Beebe, Microscale functional cytomics for studying hematologic cancers, Blood 119 (2012) e76–e85. https://doi.org/10.1182/blood-2011-10-384347.

[33] X. Su, E.W.K. Young, H.A.S. Underkofler, T.J. Kamp, C.T. January, D.J. Beebe, Microfluidic Cell Culture and Its Application in High-Throughput Drug Screening: Cardiotoxicity Assay for hERG Channels, SLAS Discovery 16 (2011) 101–111. https://doi.org/https://doi.org/10.1177/1087057110386218.

[34] E. Berthier, D.J. Beebe, Flow rate analysis of a surface tension driven passive micropump, Lab Chip 7 (2007) 1475–1478. https://doi.org/10.1039/B707637A.

[35] A.D. Proal, S. Aleman, M. Bomsel, P. Brodin, M. Buggert, S. Cherry, D.S. Chertow, H.E. Davies, C.L. Dupont, S.G. Deeks, E.W. Ely, A. Fasano, M. Freire, L.N. Geng, D.E. Griffin,

T.J. Henrich, S.M. Hewitt, A. Iwasaki, H.M. Krumholz, M. Locci, V.C. Marconi, S. Mehandru, M. Muller-Trutwin, M.M. Painter, E. Pretorius, D.A. Price, D. Putrino, Y. Qian, N.R. Roan, D. Salmon, G.S. Tan, M.B. VanElzakker, E.J. Wherry, J. Van Weyenbergh, L.M. Yonker, M.J. Peluso, Targeting the SARS-CoV-2 reservoir in long COVID, Lancet Infect Dis 25 (2025) e294–e306. https://doi.org/10.1016/S1473-3099(24)00769-2.

[36] A.D. Proal, M.B. VanElzakker, S. Aleman, K. Bach, B.P. Boribong, M. Buggert, S. Cherry, D.S. Chertow, H.E. Davies, C.L. Dupont, S.G. Deeks, W. Eimer, E.W. Ely, A. Fasano, M. Freire, L.N. Geng, D.E. Griffin, T.J. Henrich, A. Iwasaki, D. Izquierdo-Garcia, M. Locci, S. Mehandru, M.M. Painter, M.J. Peluso, E. Pretorius, D.A. Price, D. Putrino, R.H. Scheuermann, G.S. Tan, R.E. Tanzi, H.F. VanBrocklin, L.M. Yonker, E.J. Wherry, SARS-CoV-2 reservoir in post-acute sequelae of COVID-19 (PASC), Nat Immunol 24 (2023) 1616–1627. https://doi.org/10.1038/s41590-023-01601-2.

Figures

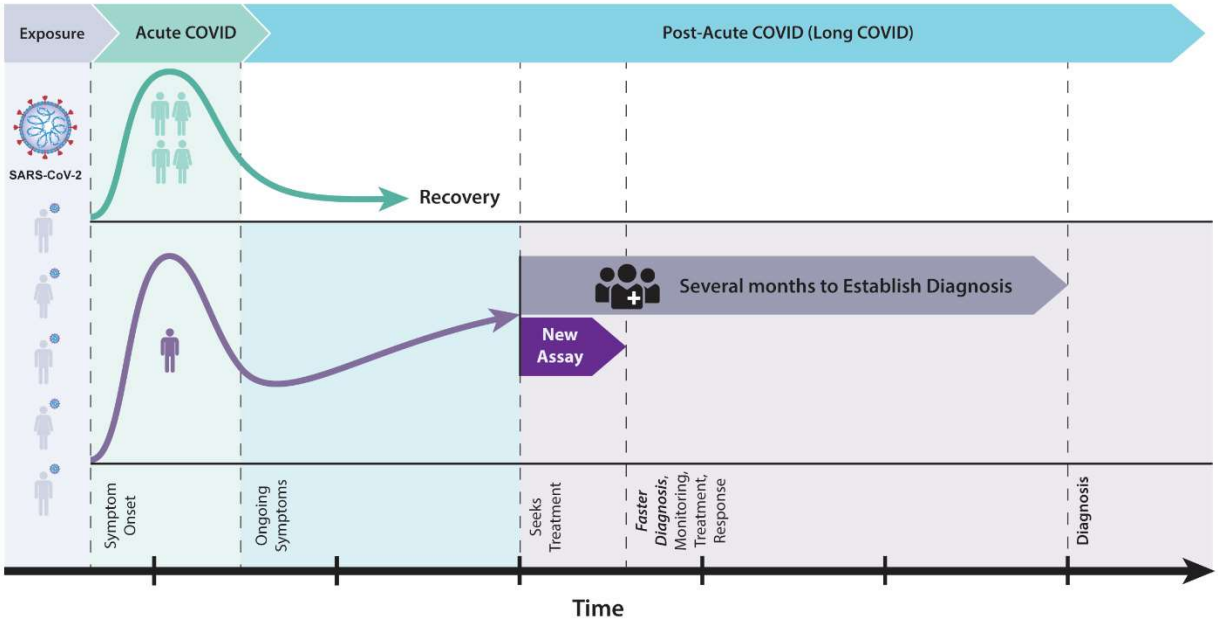

Figure 1. **Timeline of Long COVID and diagnostic challenge.** Following the acute infection phase of COVID-19, which typically spans days to weeks, 1 in 5 children experience persistent symptoms after 3 months post-infection. The condition, known as Long COVID, is difficult to diagnose because of unspecific symptoms, e.g., fatigue, brain fog, pain, and shortness of breath. Long Covid diagnosis could take months of investigations focused primarly on excluding other conditions that share the same symptoms. An assay that provides a objective metrics to help with the diagnosis of Long COVID could help reduce the diagnosis burden, help identify effective treatments, and monitor recovery.

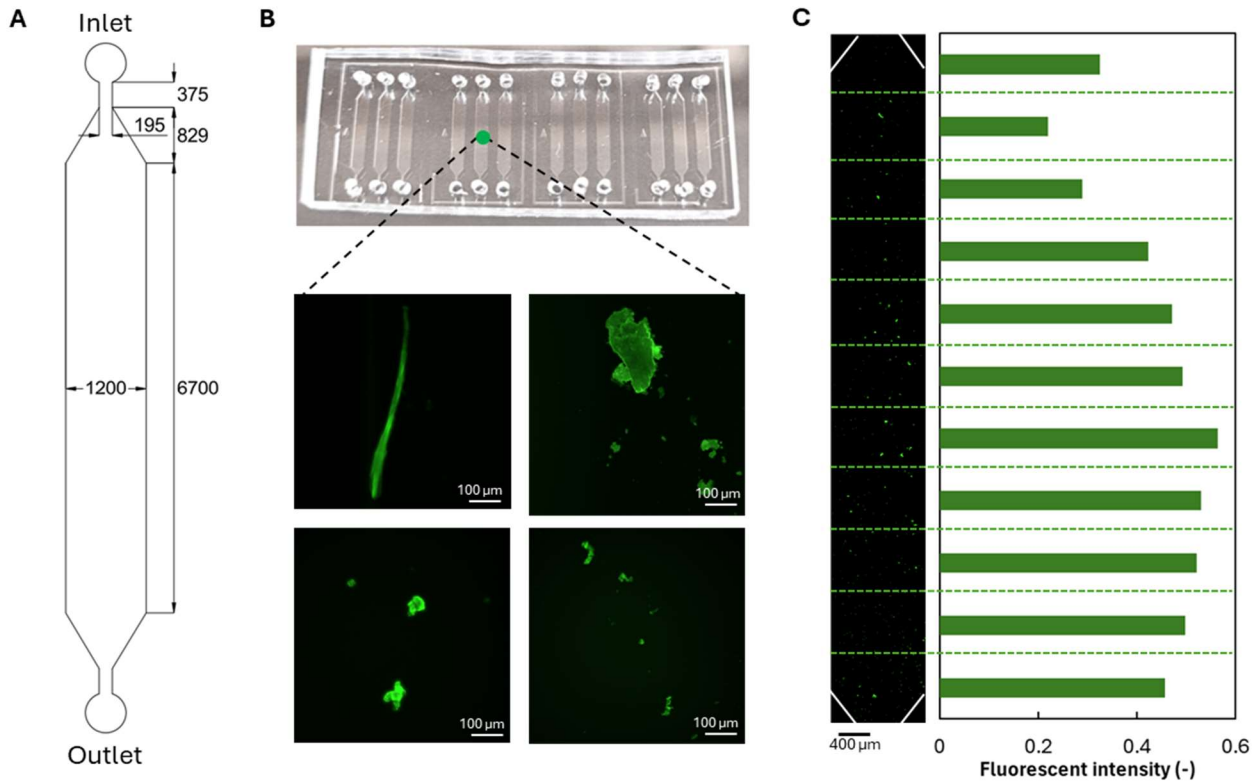

473

474

475 **Figure 2. Design of microfluidic devices for the quantification of microclots.** (A)
476 Dimensions of the microfluidic device with an inlet and outlet, and a channel for imaging
477 microclots. The height of the device is 200 µm. (B) Parallel arrangement of multiple devices on a
478 glass slide where up to 18 devices can be fitted on one slide. Representative images of
479 individual microclots in the channel, ranging from 1 - 200 µm in diameter, are shown. (C)
480 Imaging microclots in a single channel where the fluorescent intensity along the length of the
481 channel is shown. All units in µm.

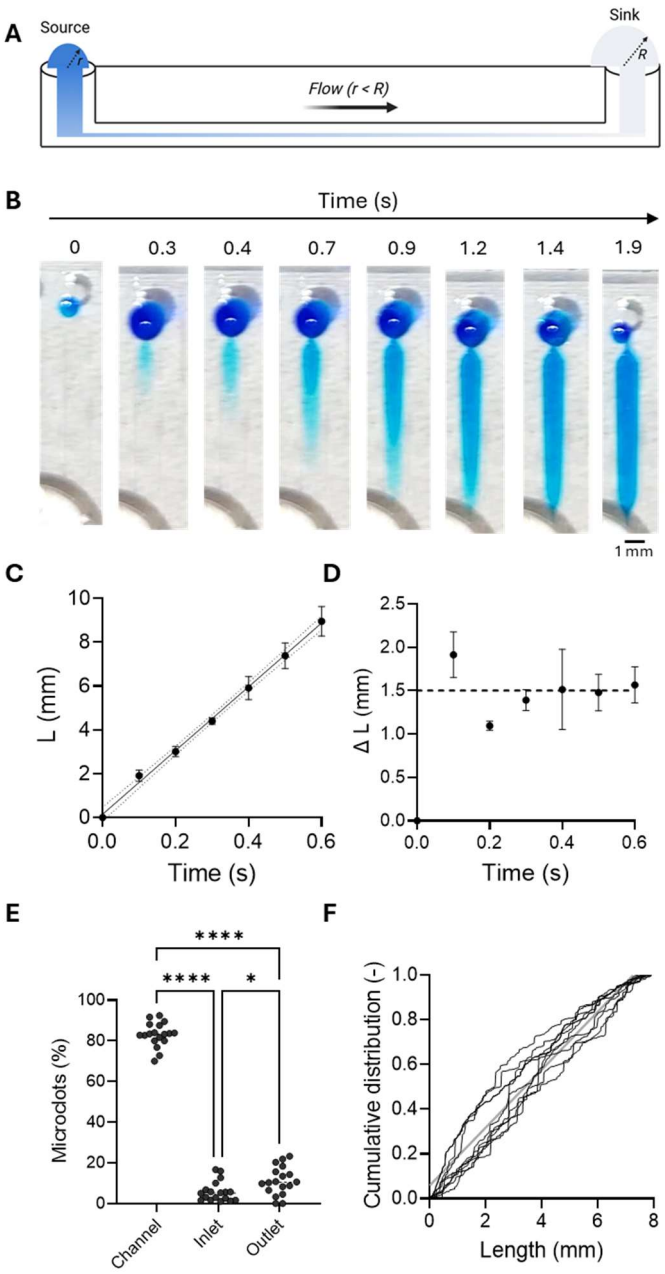

Figure 3. Passive pumping to drive flow in the microfluidic device. (A) Flow is driven by Laplace and hydrostatic forces between two droplets of different volumes connected by a conduit. The droplet with the smaller radius of curvature (*r*) has a larger pressure and drives flow towards the smaller droplet with a smaller radius (*R*) and lower pressure, which acts as a sink. (B) Blue dye is used to demonstrate the passive flow of the fluid from the smaller droplet at the inlet to the larger droplet at the outlet. (C) Fluid flow over the length (*L*) of the device over time is 15 mm/s with a linear flow rate determined using linear regression with 95% confidence interval and prediction bands (n = 3 channels) where (D) change in fluid flow over time is also shown. (E) Percentage capture of microclots in the channel of the device, compared between the inlet and outlet. (F) Cumulative distribution of microclots along the length of the device.

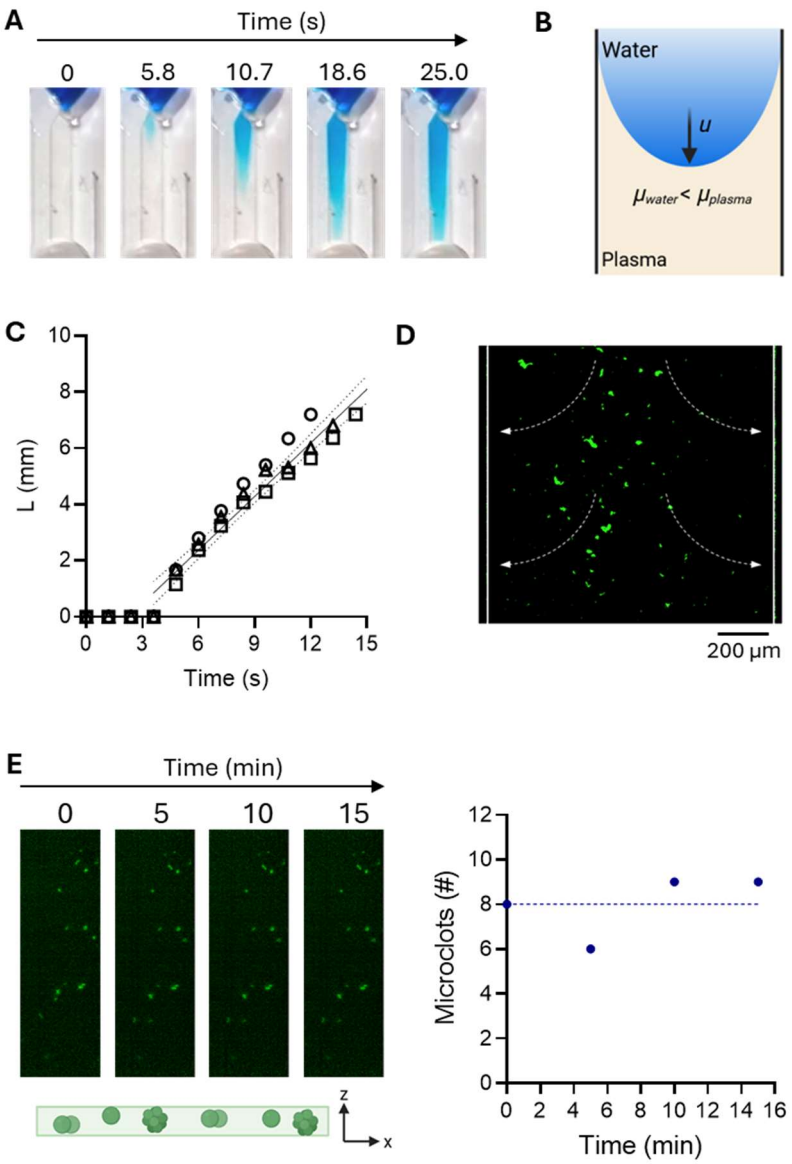

494
495

496 **Figure 4. Analysis of microclot dynamics in plasma fluid.** (A) Fluid flow of plasma over time
497 using passive flow from water-blue dye droplets. (B) Schematic of fluid-fluid interface in
498 microchannels where the viscosity of plasma is lower than that of water. (C) Travelling distance
499 of fluid front along the length of the device over time with a velocity of 0.65 mm/s determined
500 using linear regression with 95% confidence interval and prediction bands (n = 3 channels). (D)
501 Lateral distribution of microclots using passive flow. (E) Tracking the number of microclots over
502 time at a single z-stack near the bottom of the device after flowing fluid through the device to
503 test settling effects of microclots.

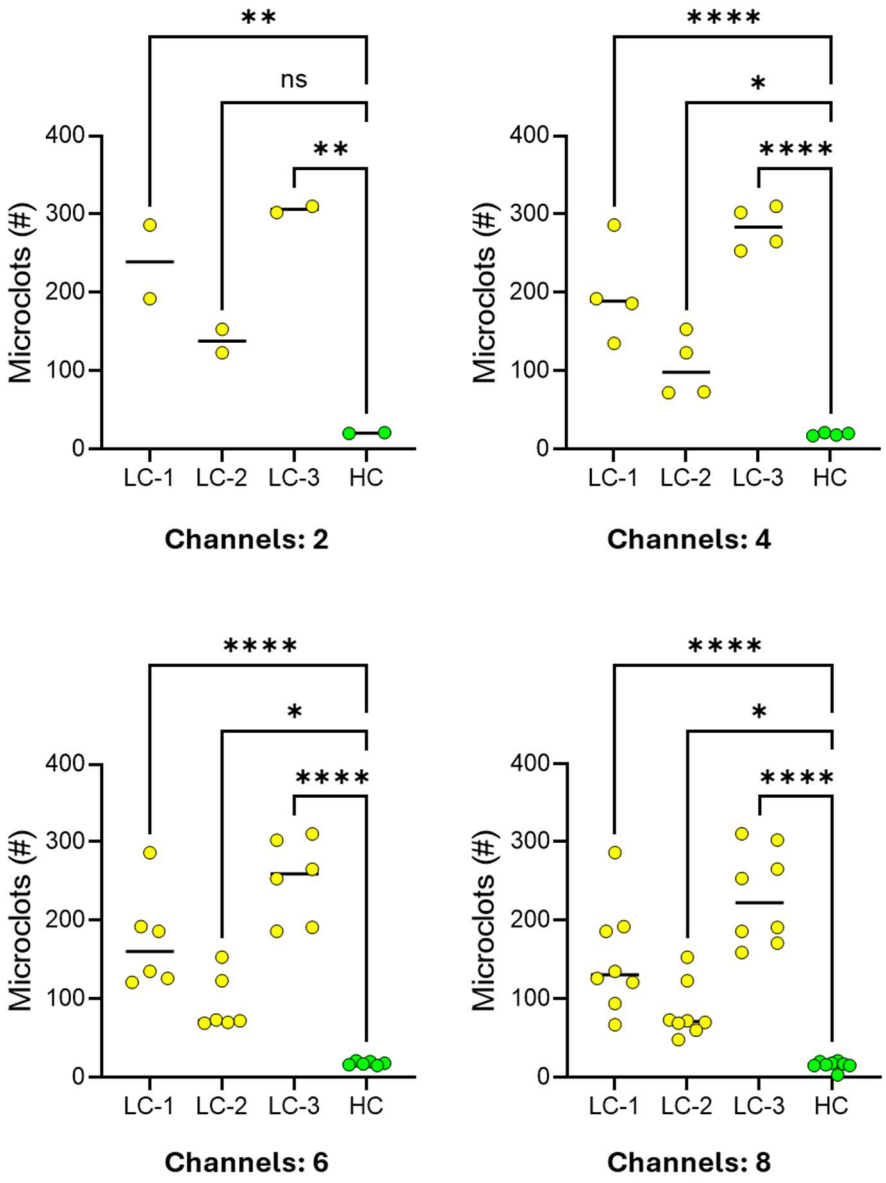

504
505
506

507 **Figure 5. Optimization of channel number.** Determining the number of channels to use per
508 sample by comparing 3 LC samples with one HC sample. Channel numbers tested range from 2
509 to 8. Statistical analysis was carried out using one-way ANOVA with a 0.05 confidence level.
510

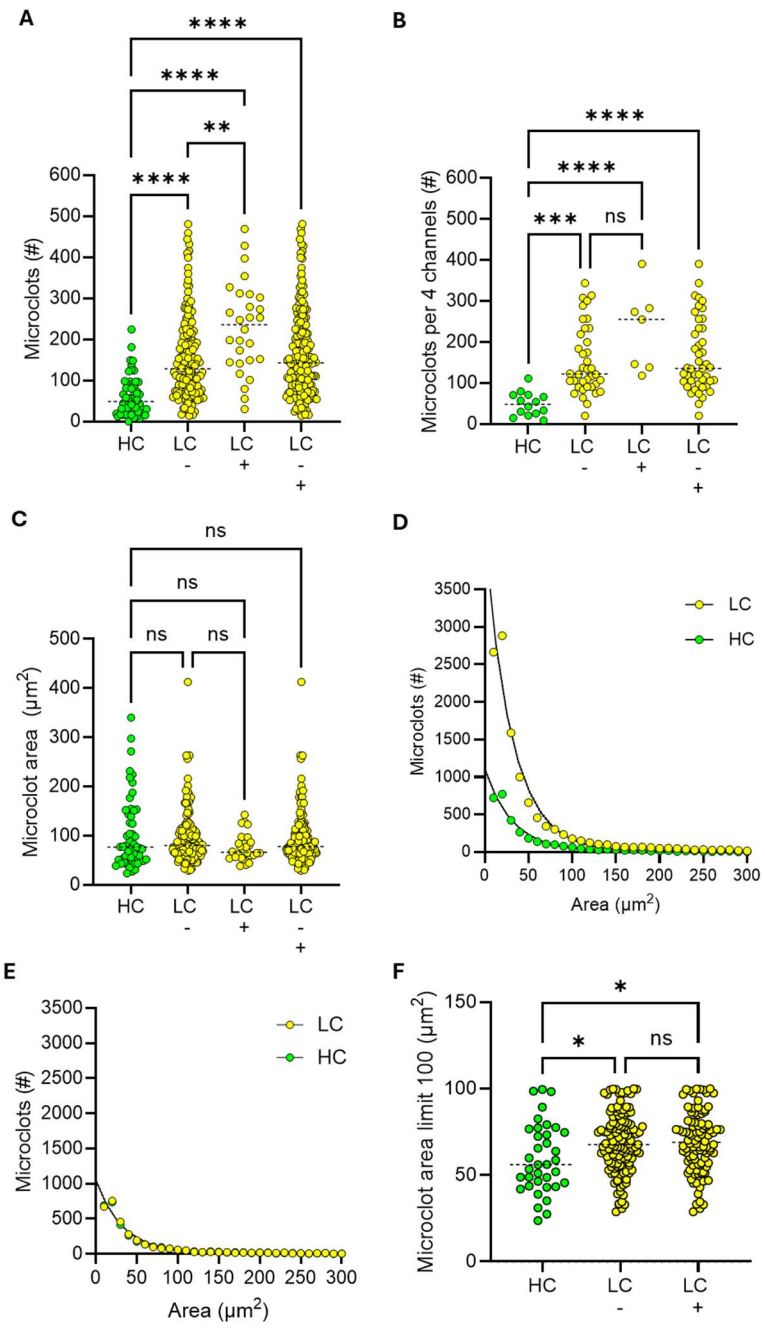

Figure 6. Quantifying the number and size of microclots in Long COVID (LC) samples and healthy controls (HC). (A) Number of microclots for LC (+) samples (n = 7 samples), LC (-) samples (n = 38 samples) and HC (n = 14 samples). Data is shown for microclots per channel where four channels are used for each sample and (B) for the number of microclots averaged across four channels per sample. (C) Microclot area for LC (+), LC (-) and HC samples per channel, where four channels are used per sample. (D) Histogram showing the distribution of the number of microclots for LC (LC+ and LC-) and HC samples, with bin area set to 10 µm^2 for all microclots and (E) normalized for the same number of microclots. (F) Microclot area for LC (+), LC (-) and HC samples, where the maximum area is set to 100 µm^2. Statistical analysis was carried out using one-way ANOVA with a 0.05 confidence level.

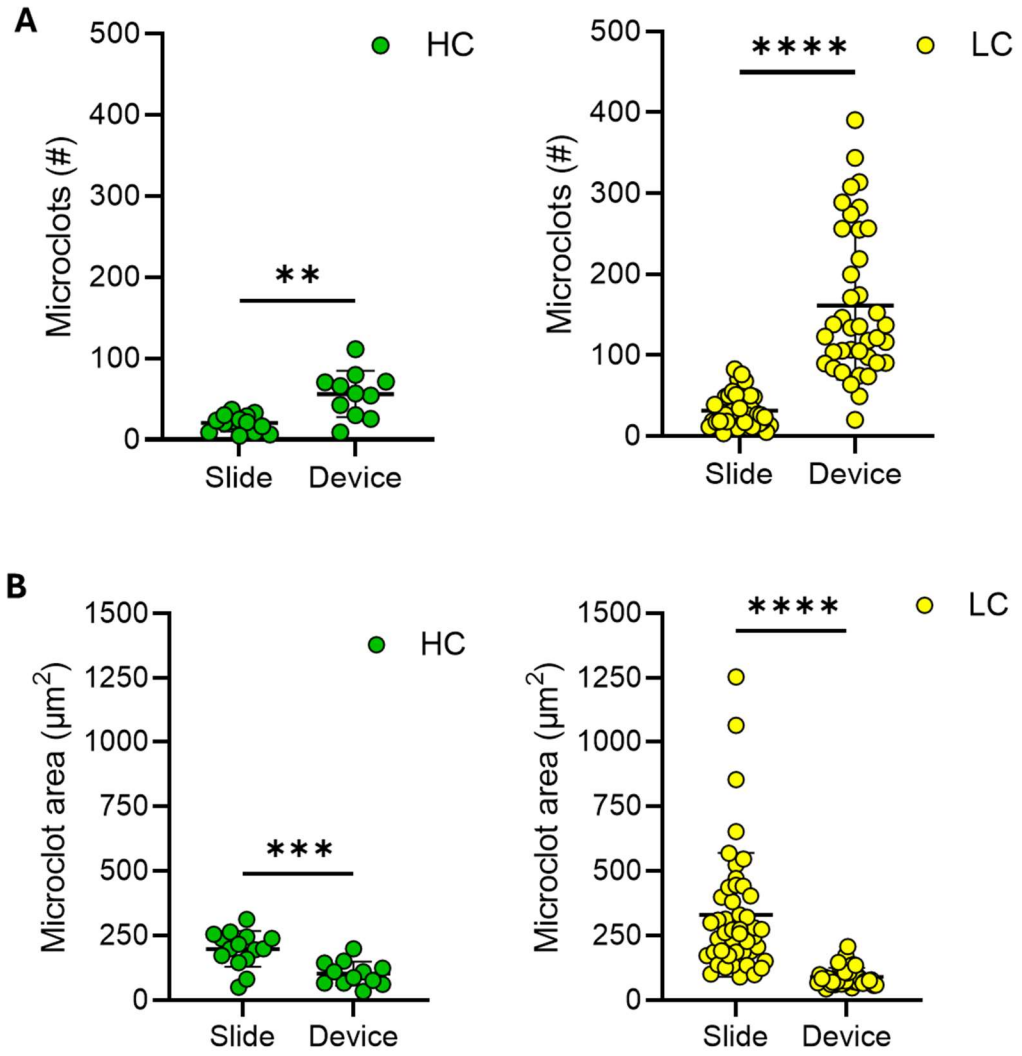

Figure 7. Quantifying clots using microfluidic devices compared to standard microscope slides. (A) Count and (B) area of microclots for HC (n = 14 and n = 11 for devices) and LC samples (n = 46 for slides and n = 39 for devices). Statistical analysis was carried out using a two-tailed paired t-test with a 0.05 confidence level.

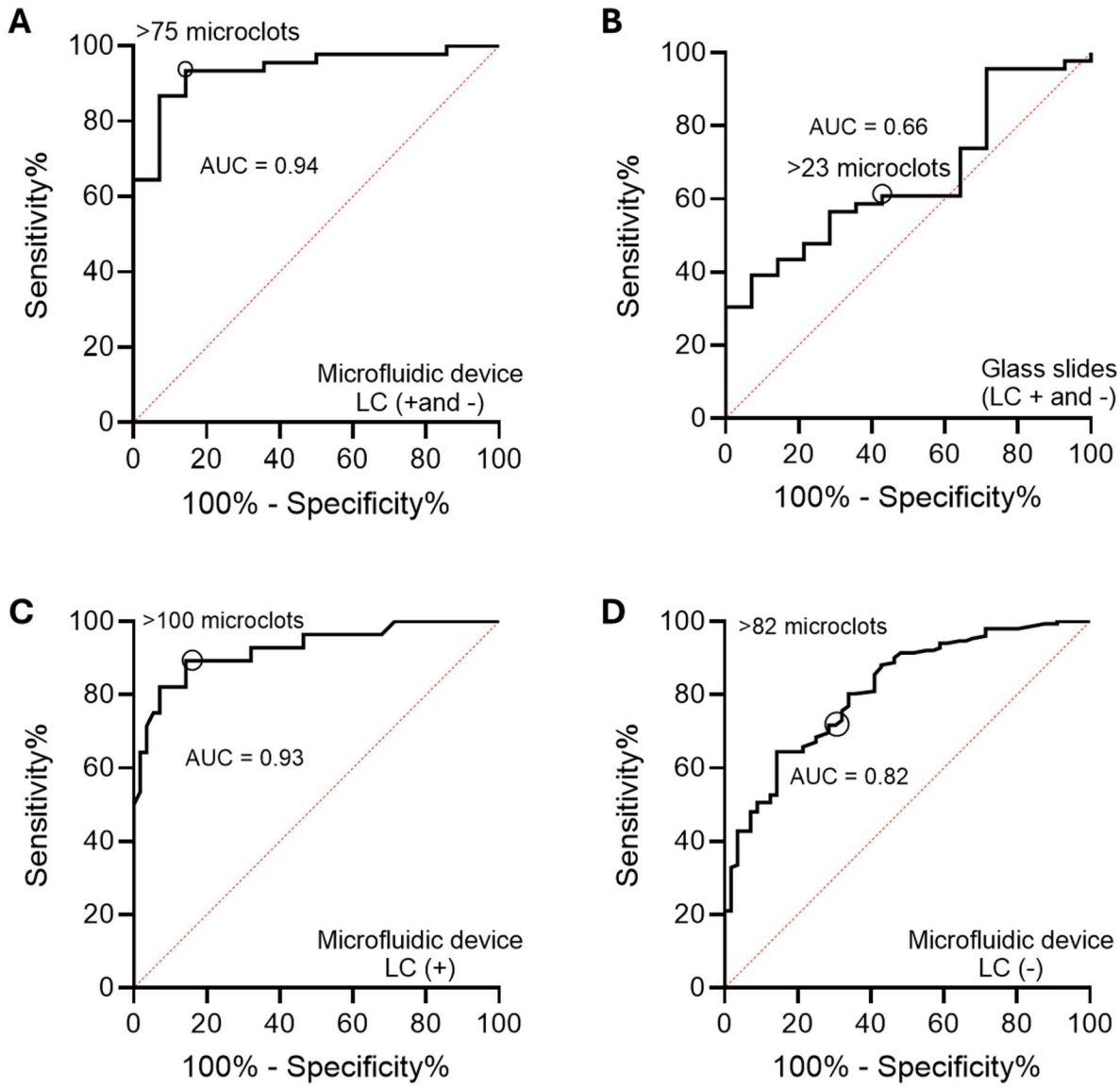

528

529 **Figure 8. Receiver operating curve (ROC) for the new microfluidic assay and the current**
530 **microclot assessment method.** (A) When microclots were counted in the microfluidic devices,
531 using four channels per sample, we calculated an optimal threshold for differentiating healthy at
532 an average of 75 clots/sample. AOC was 0.94, with corresponding LC Sensitivity: 91%,
533 Specificity: 86% (n = 45 LC samples, n =14 Healthy samples). (B) In the current method of
534 counting on slides, the threshold count was 23 clots/sample. AOC was 0.66, with
535 corresponding LC Sensitivity: 61%, Specificity: 57% (n = 45 LC samples, n = 14 Healthy
536 samples). (C) For LC (+) only samples in microfluidic devices, the AUC was 0.93, Sensitivity:
537 89%, Specificity: 86% (n = 28 channels). (D) For LC (-) only samples in microfluidic devices, the
538 AUC was 0.82, Sensitivity: 72%, Specificity: 71% (n = 152 channels).

Tables

Table 1. Participant demographics of participants enrolled in the validation of the LC assay

Total enrolled (n = 59)	**Healthy (n = 14)**	**Long COVID (n=45)**		
		All LC samples (n=45, 100%)	Spike negative (n = 38, 84%)	Spike positive (n = 7, 16%)
Age, mean years (min, max)	8.3 (0.9, 11)	16.7 (8.6, 51).	17.0 (8.6, 51)	15.2 (8.6, 19)
Sex, n (%)				
Female	6 (43%)	23 (51%)	18 (47%)	5 (71%)
Male	8 (57%)	22 (49%)	20 (53%)	2 (29%)
Race, n (%)				
White or Caucasian	7 (50%)	39 (89%)	34 (89%)	5 (71%)
Black or African American	1 (7%)	1 (2%)	1 (3%)	0 (0%)
Asian	3 (21%)	1 (2%)	0 (0%)	1 (14%)
Other	3 (21%)	3 (7%)	2 (5%)	1 (14%)
Ethnicity, n (%)				
Hispanic or Latino	4 (29%)	7 (15%)	7 (18%)	0 (0%)
Not Hispanic or Latino	10 (71%)	38 (85%)	31 (82%)	7 (100%)

Supplementary Files

This is a list of supplementary files associated with this preprint. Click to download.

- SupplementaryVideoV1.mp4